

# Enhancing crystal growth using polyelectrolyte solutions and shear flow

<https://doi.org/10.1038/s41586-020-2042-1>

Received: 3 April 2019

Accepted: 2 December 2019

Published online: 4 March 2020

 Check for updates

Jian-Ke Sun<sup>1,3,6</sup>, Yaroslav I. Sobolev<sup>1,6</sup>, Weiyi Zhang<sup>4</sup>, Qiang Zhuang<sup>1,5</sup> & Bartosz A. Grzybowski<sup>1,2</sup>✉

The ability to grow properly sized and good quality crystals is one of the cornerstones of single-crystal diffraction, is advantageous in many industrial-scale chemical processes<sup>1–3</sup>, and is important for obtaining institutional approvals of new drugs for which high-quality crystallographic data are required<sup>4–7</sup>. Typically, single crystals suitable for such processes and analyses are grown for hours to days during which any mechanical disturbances—believed to be detrimental to the process—are carefully avoided. In particular, stirring and shear flows are known to cause secondary nucleation, which decreases the final size of the crystals (though shear can also increase their quantity<sup>8–14</sup>). Here we demonstrate that in the presence of polymers (preferably, polyionic liquids), crystals of various types grow in common solvents, at constant temperature, much bigger and much faster when stirred, rather than kept still. This conclusion is based on the study of approximately 20 diverse organic molecules, inorganic salts, metal–organic complexes, and even some proteins. On typical timescales of a few to tens of minutes, these molecules grow into regularly faceted crystals that are always larger (with longest linear dimension about 16 times larger) than those obtained in control experiments of the same duration but without stirring or without polymers. We attribute this enhancement to two synergistic effects. First, under shear, the polymers and their aggregates disentangle, compete for solvent molecules and thus effectively ‘salt out’ (that is, induce precipitation by decreasing solubility of) the crystallizing species. Second, the local shear rate is dependent on particle size, ultimately promoting the growth of larger crystals (but not via surface-energy effects as in classical Ostwald ripening). This closed-system, constant-temperature crystallization driven by shear could be a valuable addition to the repertoire of crystal growth techniques, enabling accelerated growth of crystals required by the materials and pharmaceutical industries.

Although the phenomena we describe are observed even in solutions stirred by an ordinary magnetic stir bar (Supplementary Video 1), most experiments were performed in a standardized Couette cell, with a gap of  $d = 1$  mm and the inner cylinder ( $r_1 = 4$  mm in radius) rotating at a constant angular velocity, usually  $\omega = 400$  rpm, corresponding to shear rate  $\dot{\gamma} = 167$  s<sup>-1</sup> (Fig. 1) but down to 60 rpm in some control experiments (see Fig. 4a). In all experiments, the Reynolds number (for the inner cylinder)  $Re = r_1\omega d/\nu$  (where  $\nu$  is kinematic viscosity) was smaller than 2, ensuring simple Couette flow rather than the more complicated flow regimes expected for  $Re \geq 100$  (ref. 15). The typical procedure described here is for simple trimesic acid (TA), but is similar to that for other systems discussed later (see Fig. 3 and Supplementary Information section 2.2).

In brief, we start by mixing an undersaturated solution of a crystallizing substance in a solvent (47 mg of TA per 0.4 ml of dimethylformamide

(DMF)) with 0.35 ml of the same solvent containing a polyionic liquid polymer (300 mg of poly(3-cyanomethyl-1-vinylimidazolium bis(trifluoromethanesulfonyl)imide); henceforth PIL-1, molecular weight  $4.02 \times 10^5$  g mol<sup>-1</sup>, Fig. 2; Supplementary Video 2). The concentration of TA in the 0.75 ml of solution thus prepared exceeds the saturation level by 15.5 mg, even though approximately twice as much TA can be dissolved in pure DMF (92.6 mg per 0.75 ml), which indicates that PIL-1 and TA are competing for shared DMF. The TA/PIL-1/DMF mixture is poured into the Couette cell and, when the inner cylinder begins to rotate, is subject to uniform shear flow (Supplementary Information section 4.4). First, needle-shaped crystals become visible to the naked eye after about 30 s of rotation, move with the fluid, and gradually grow to about 440  $\mu$ m after 10 min and about 740  $\mu$ m after one hour (Fig. 1c and blue line in Fig. 1d). Spectroscopic signatures (from powder X-ray diffraction and <sup>1</sup>H nuclear magnetic resonance (NMR) of washed and

<sup>1</sup>Center for Soft and Living Matter, Institute for Basic Science, Ulsan, South Korea. <sup>2</sup>Department of Chemistry, Ulsan National Institute of Science and Technology, Ulsan, South Korea. <sup>3</sup>School of Chemistry and Chemical Engineering, Beijing Institute of Technology, Beijing, China. <sup>4</sup>Department of Materials and Environmental Chemistry, Stockholm University, Stockholm, Sweden.

<sup>5</sup>Department of Applied Chemistry, School of Natural and Applied Sciences, Northwestern Polytechnical University, Xi'an, China. <sup>6</sup>These authors contributed equally: Jian-Ke Sun, Yaroslav I. Sobolev. ✉e-mail: nanogryzbowski@gmail.com

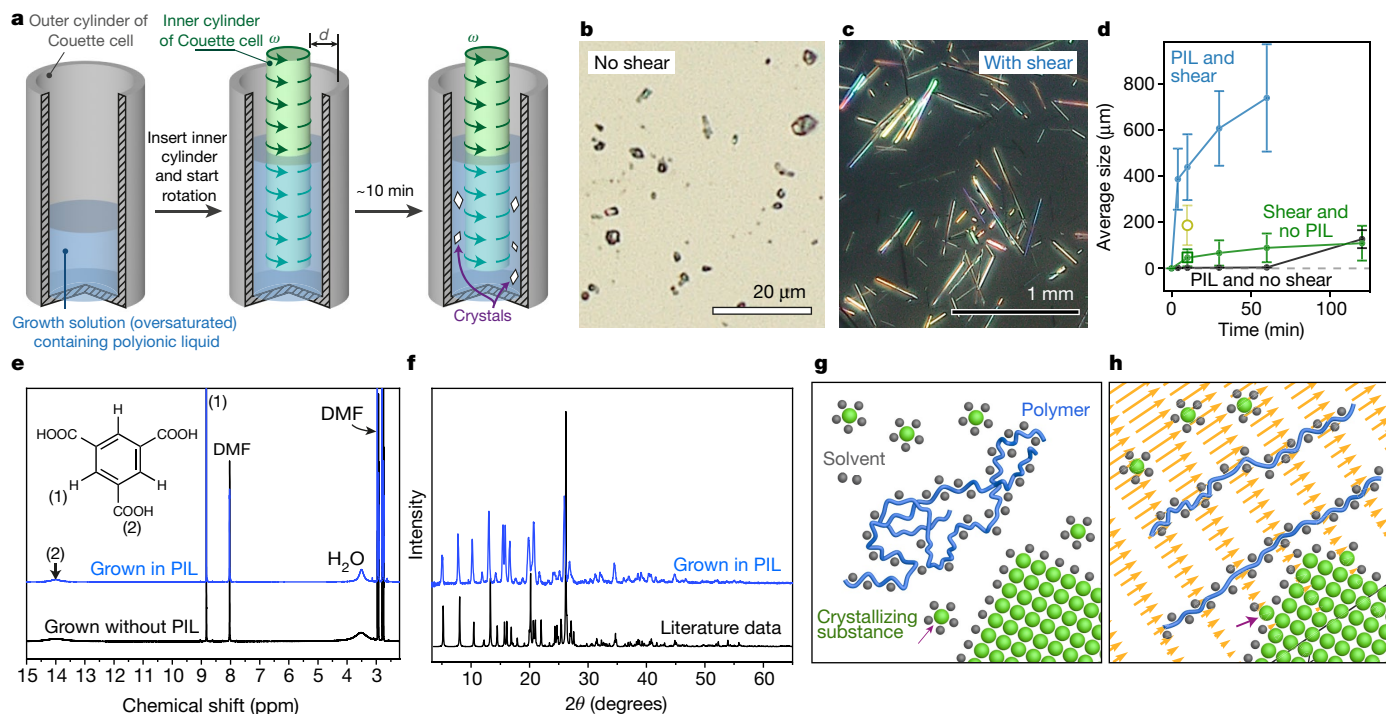


**Fig. 1 | Shear-enhanced growth of TA crystals in the presence of an ionic polymer.** **a**, Illustration of experimental set-up. **b, c**, Optical images of TA crystals grown within 10 min from the same TA/PIL-1/DMF solution without (**b**) and with (**c**) applied shear. We note that the scale bars are different. Image **b** is taken with bright-field illumination; image **c** is taken with crossed polarizers. **d**, Average sizes of TA crystals increasing with time under shear in the presence of PIL-1 (blue; statistics based on  $n = 49$ –58 crystals analysed for each time point), without shear but in the presence of PIL-1 (black;  $n = 35$ –43), and with shear in pure DMF (green;  $n = 236$ –391). Error bars indicate standard deviations of sizes, not the errors of the mean. The green line corresponds to control experiments without PIL-1 but under shear, in which 15.5 mg oversaturation of TA in DMF was achieved by adding 108.1 mg of TA powder to 0.75 ml of pure DMF before application of shear (we verified separately that the saturation level of TA in pure DMF is 92.6 mg per 0.75 ml). The outcome was not sensitive to the time it took most of the TA powder to dissolve: the average size of the crystals obtained was the same in another experiment whereby 85 mg of TA was first completely dissolved in 0.75 ml of pure DMF at 25 °C, and an additional 23 mg of TA powder was added to the solution immediately before the start of cell rotation (open green square). Finally, the open yellow circle corresponds to

an experiment in which 108.1 mg of TA (but no PIL-1) was first completely dissolved in 0.75 ml of DMF at a slightly elevated temperature of 36 °C and then subjected to shear at 25 °C for 10 min. In other words, oversaturation in this experiment was achieved by cooling. In all experiments with non-zero shear, the mean shear rate was  $\dot{\gamma} = 167 \text{ s}^{-1}$ . **e**,  $^1\text{H}$  NMR spectra of the washed and redissolved TA single crystals grown in PIL-1/DMF at  $\dot{\gamma} = 167 \text{ s}^{-1}$  shear flow (blue) and by evaporation of DMF from the TA/DMF solution without any PIL (black). The chemical structure in the inset is TA. **f**, Powder X-ray diffraction spectra of TA crystals grown in PIL-1/DMF at  $\dot{\gamma} = 167 \text{ s}^{-1}$  shear flow (blue) compared to literature data<sup>40</sup> for pure TA crystals grown in DMF (black). **g, h**, Scheme of the conjectured mechanism: the polymer (blue) and the crystallizing substance (green) compete for shared solvent (grey). When shear flow is absent (**g**), the amount of solvent sufficient to solvate the entangled polymer is lower than that to solvate the polymer disentangled by shear flow (**h**). The disentangling polymer ‘steals’ this additional solvent from the molecules of the crystallizing substance, causing these molecules to attach to the nearby crystal (the purple arrow in both panels points to the same particle). Orange arrows illustrate the vector field of fluid velocity in the case of a mean shear flow. For effects of shear on nucleation, see the discussion in the main text and Fig. 4.

redissolved crystals in Fig. 1e, f; see also Fourier-transform infrared spectroscopy in Supplementary Fig. 13 and single-crystal X-ray diffraction in Supplementary Information section 2), are free of any PIL-1, match the spectra of TA-DMF crystals reported in the literature, and are of crystallographic quality (in terms of single-crystal X-ray diffraction) as good as those of TA crystals grown by conventional recrystallization or solvent evaporation (Supplementary Fig. 12c). In sharp contrast, if the same solution or protocol is used but no rotation is applied, the ill-shaped (Fig. 1b) crystals are only about 2  $\mu\text{m}$  long after 10 min of growth (black line in Fig. 1d). When PIL-1 is absent but shear is applied, the needle-like crystals are about 44  $\mu\text{m}$  long at 10 min (green line in Fig. 1d). None of these and also none of some other control experiments summarized in Fig. 1d (see also Fig. 4 for growth from powders using different shear rates, monomers or polymers of different length) yield crystals of sizes comparable to those grown under shear and with PIL-1 present.

Importantly, similar growth enhancement is observed for other, structurally diverse substances. This claim is supported by the size comparisons (shear + PIL versus no-shear + PIL, same growth times, all at room temperature) in Fig. 3a as well as the corresponding images

of crystals of various small molecules, inorganic salts, metal–organic complexes, and even some proteins (Fig. 3b and Supplementary Figs. 12–35). The average increase in the longest linear dimensions of the crystals is about 16-fold, as high as 42-fold for NaI, 171-fold for TA, and never smaller than 2-fold. The phases and crystallinities of the crystals match those grown over much longer times via traditional solvent evaporation (crystallinities are annotated as percentages in Fig. 3a and plotted in Supplementary Fig. 12; powder X-ray diffraction spectra are shown in Supplementary Figs. 16–28 and 31–35). BET surface areas of porous functional materials are improved with respect to synthesis by conventional methods (without PIL) by 51% for both the porous organic cage **17** and the covalent organic framework **20**, and by 24% for the metal–organic framework **19**. Although absolute values generally depend on the synthetic protocol and activation method, the increase we observe is systematic (with the same activation method for each pair; see Supplementary Fig. 41), and may reasonably be attributed to defects present in the samples grown under shear<sup>16</sup>.

Regarding the choice of polymers used in the growth experiments (Fig. 2a), uncharged ones—such as poly(methyl methacrylate), PMMA, or polyvinylidene fluoride, PVDF—also give similar results

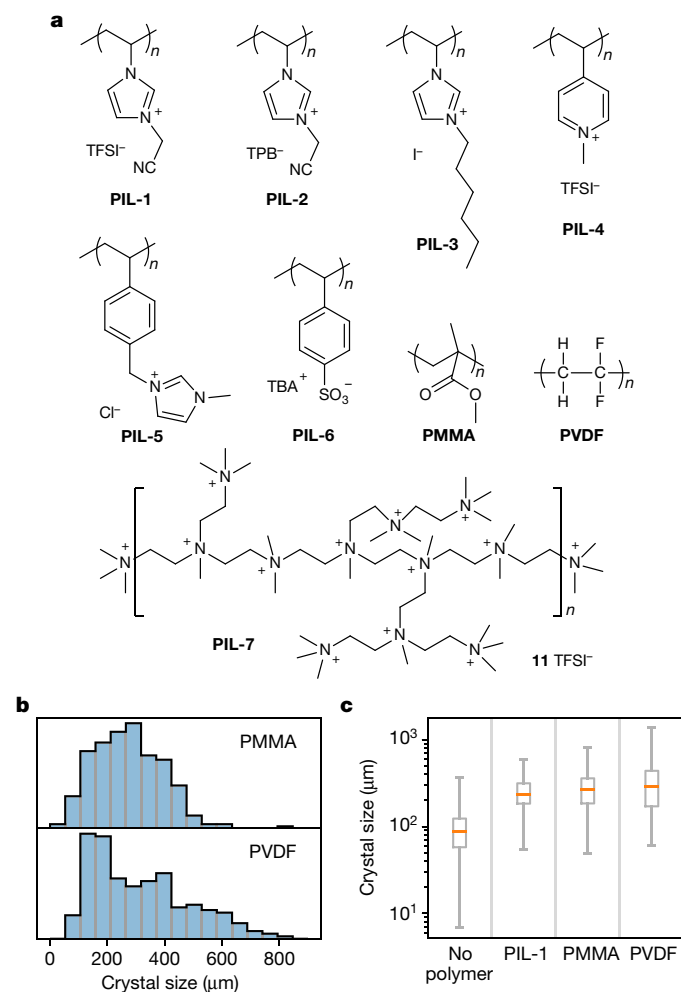


**Fig. 2 | Various polymers used for shear-enhanced crystallization.** **a**, Most reliable results were obtained using polyionic liquid polymers bearing either positive (**PIL-1**–**PIL-5** and **PIL-7**) or negative (**PIL-6**) charges. **PIL-1** is poly(3-cyanomethyl-1-vinylimidazolium bis(trifluoromethanesulfonyl)imide); **PIL-2** is poly(3-cyanomethyl-1-vinylimidazolium tetraphenylborate); **PIL-3** is poly(3-hexyl-1-vinylimidazolium iodide); **PIL-4** is poly(1-methyl-4-vinylpyridinium bis(trifluoromethanesulfonyl)imide); **PIL-5** is poly(3-methyl-1-(4-vinylbenzyl)imidazolium chloride); **PIL-6** is poly(tetrabutylammonium 4-styrenesulfonate); and **PIL-7** is quaternary ammonium polyethyleneimine. For synthetic details and characterization, see Supplementary Information section 1. PMMA and PVDF were also used but were not suitable for all solutes, with some of which (for example, TA and NaI) they gelled. (**11** refers to NaI). **b**, Representative size distributions of TA crystals grown from approximately 2- $\mu\text{m}$  TA powder in PMMA/DMF and PVDF/DMF. **c**, Box plots of crystal sizes for the systems in **b** as well as for the PIL-1 and no-polymer conditions. For all cases, the concentration of polymer was 75 mg per 0.75 ml, growth time 3 h, and mean shear rate  $\dot{\gamma} = 85 \text{ s}^{-1}$  (that is, twice as low as in Fig. 1; for effects of  $\dot{\gamma}$  on crystal size, see Fig. 4). Molecular weights were  $996 \text{ kg mol}^{-1}$  (PMMA),  $275 \text{ kg mol}^{-1}$  (PVDF), and  $402 \text{ kg mol}^{-1}$  (PIL-1). In **c**, the elements of the box plots are: 25% and 75% quartiles (edges of the boxes), median (midlines), and maximum/minimum values (whiskers). Numbers of crystals on which these statistics are based are: no PIL, 248; PIL-1, 235; PMMA, 284; PVDF, 242.

(see Fig. 2b, c), although with some solutes (for example, TA and NaI) they gelate. Both negatively and positively charged PILs are more robust, confirming previous reports that ionic liquids are versatile solvents compatible with a wide range of solutes<sup>17,18</sup> and suitable for growing crystals<sup>19</sup> (though never before in shear flow). Conveniently, with the selection of PILs shown in Fig. 2a, we have been able to make our method compatible with solvents ranging from polar (DMF, dimethyl

sulfoxide (DMSO), water and methanol) to less polar (dichloromethane, DCM) by changing the polarity (or sign) of the pendant-chain charges or by varying counterions from small halogen anions to the large tetrabutylammonium (TBA) cation (see specific experimental procedures in Supplementary Information section 2.2).

To better understand the mechanism of shear-enhanced crystal growth, we performed a series of experiments in which we systematically varied the shear rates and polymer chain length. In these experiments, summarized in Fig. 4, we aimed to eliminate any effects of initial nucleation, whose dependence on shear may be convoluted and whose mechanisms are still unclear (see refs. <sup>10,11</sup> and references therein). Accordingly, we grew the crystals by ripening of TA powders (average particle size  $2 \pm 0.5 \mu\text{m}$ ) in PIL-1/DMF, in contrast to growing the crystals from uniform solutions (see above and Figs. 1, 3). The histogram in Fig. 4a provides evidence that, when other parameters are kept constant, the size of the crystals increases with increasing shear rate and already at  $\dot{\gamma} = 167 \text{ s}^{-1}$  further growth becomes limited by the 1-mm gap between the walls of the Couette cell. The distributions in Fig. 4b demonstrate that at a given shear rate, for the same concentration of PIL-1 monomers and same excess (15.5 mg per 0.75 ml of DMF) of TA mass over saturation level (Fig. 4c), crystal sizes increase when the lengths of the PIL-1 polymer chains increase. In parallel, the rheological data in Fig. 4d demonstrate that the viscosities of the solutions also increase in the same order, while the solubility  $c_s$  of TA plotted in Fig. 4c decreases. This is an important observation as it strongly indicates that the phenomena we describe cannot be rationalized simply by mixing accelerating transport between crystallites and thus facilitating Ostwald ripening. Both diffusion of macromolecules and mixing slow down in viscous media, whereas the diffusion of small molecules in polymer solutions is either unaffected by increased polymer length or slows down slightly<sup>20,21</sup>. The solubility  $c_s$  of TA in PIL-1/DMF solutions is 3.5 times lower than in pure DMF and 1.7 times lower than in monomer/DMF solution (Fig. 4c). Therefore, from the scaling arguments presented in Supplementary Information section 7, we would expect that classical, transport-limited Ostwald ripening of TA in PIL-1/DMF mixtures is at least  $(3.5)^{3/7} \approx 1.7$  times slower than in pure DMF and  $(1.7)^{3/7} \approx 1.25$  times slower than in monomer/DMF solution (opposite to the actual trend in Fig. 4b) and should slow down with (or, at least, not be affected by) the polymer's molecular weight, which is not the case. We also ruled out potential thermal effects from viscous heating (see Supplementary Information section 4.3). Finally, the curves in Fig. 4d, e capture the decrease of viscosity with increasing shear rate. This so-called 'shear thinning' can be ascribed to polymers or their aggregates disentangling or unfolding in elongational and shear flows; this phenomenon was predicted by de Gennes<sup>22</sup> and experimentally confirmed by analyses of bulk properties<sup>23–26</sup> and even by direct single-molecule imaging<sup>27</sup>. We note that the decrease in viscosity shown in Fig. 4d, e, owing to some changes of polymer solution microstructure, necessarily begins at shear rates below  $10 \div 100 \text{ s}^{-1}$ , and therefore these local microstructure changes must be activated by the shear ( $25 \div 167 \text{ s}^{-1}$ ) that we apply in crystal growth experiments (for a detailed discussion of rheology, see Supplementary Information section 6). In this context, we observe that prolonged shearing of the PIL-1/DMF solution reduces the number-averaged hydrodynamic radius  $r_h$  observed by DLS (for example, from about 800 nm to 60 nm at  $\dot{\gamma} = 167 \text{ s}^{-1}$  for 3 h), although these experiments themselves do not provide detailed insight into the microscopic changes in the polymer's structure (disentanglement, unfolding, breaking of gel-like structures or destruction of the aggregates the PILs are known to form<sup>28</sup> and which may break under shear flow<sup>29</sup>).

All of these observations substantiate a plausible mechanism involving (1) shear-dependent solvation changes and (2) differences in the local shear rates around larger (rather than smaller) crystals. Specifically, as the polymer chains disentangle or their aggregates distort or break under shear, they become better exposed to the solvent and

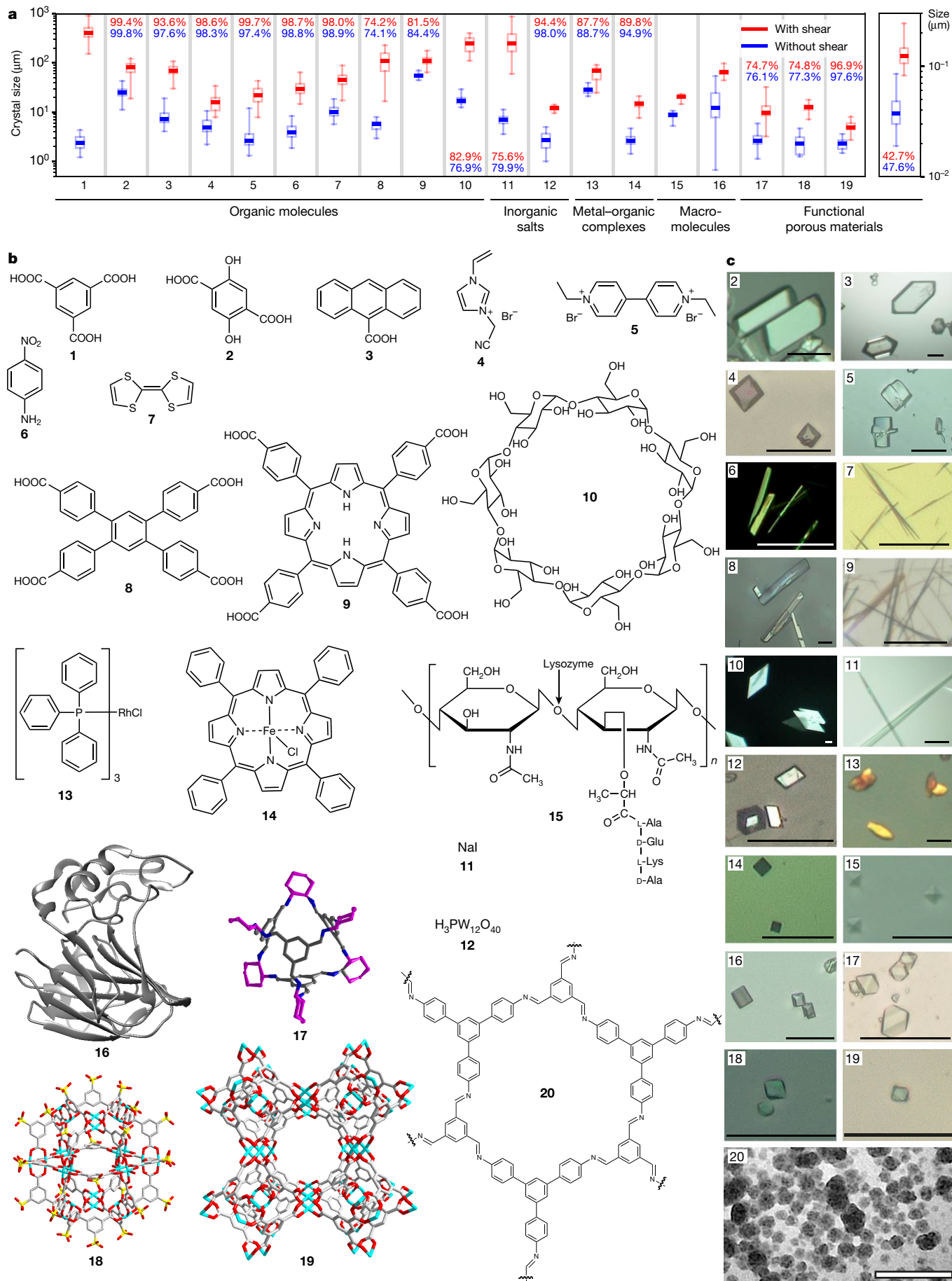
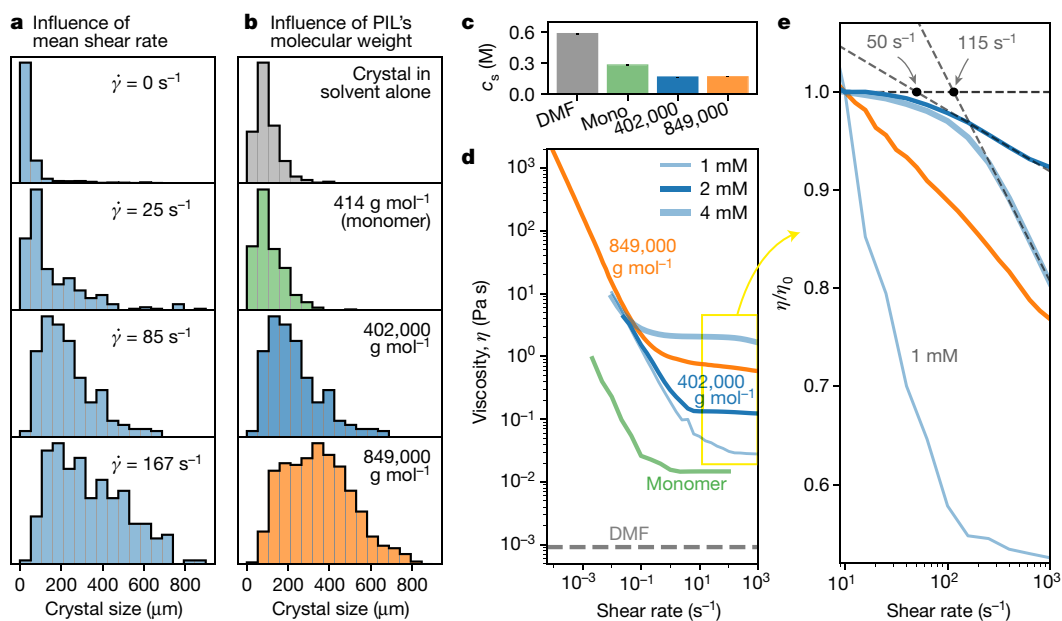


Fig. 3 | See next page for caption.

**Fig. 3 | Shear-enhanced growth of additional 19 different crystals in the presence of polyionic liquids.** **a**, Sizes of crystals (note logarithmic vertical scale) obtained with shear (red) and without shear (blue) under otherwise identical conditions. The elements of the box plots are: 25% and 75% quartiles (edges of the box), median (midline), and maximum/minimum values (whiskers). Numbers of crystals analysed for each substance are given below (along with experimental conditions) and denoted as  $n_1$  for with-stirring conditions and  $n_2$  for no-stirring conditions. Crystal quality (percentages of crystalline phase evaluated by powder X-ray diffraction analysis) is indicated by numbers on bar plots, in red font for crystals grown with PIL under shear and in blue font for crystals grown with a conventional method (see Supplementary Figs. 11, 12 for details). **b, c**, The specific substances we tested (**b**) and the crystals they typically grow under shear (scale bars = 50  $\mu\text{m}$ , with the exception of **20**, where the scale bar is 0.5  $\mu\text{m}$ ) (**c**). All crystals were grown in a Couette cell (Fig. 1a; see Supplementary Information section 5 for cell design) with gap  $d = 1\text{ mm}$  and at a constant shear rate  $\dot{\gamma} = 167\text{ s}^{-1}$  ( $\omega = 400\text{ rpm}$ ). Various PILs (both positively and negatively charged) were used (chosen to be miscible with the solute or solvent) and their molar concentrations are given in terms of repeat units. Unless otherwise specified, the solvent was DMF.  $C$  values are the concentrations of the crystallizing solutes. Times are those of growth under shear and were chosen such that the formation of first crystals could be discerned, in many cases by the naked eye. Detailed experimental conditions, size distributions and additional images of crystals grown with and without shear can be found in Supplementary Information section 2.1, TA, growing

time 10 min ( $C = 0.30\text{ M}$ ,  $C_{\text{PIL-1}} = 1\text{ mM}$ ,  $n_1 = 58$ ,  $n_2 = 35$ ). **2**, 2,5-dihydroxyterephthalic acid, 10 min ( $C = 0.2\text{ M}$ ,  $C_{\text{PIL-1}} = 0.97\text{ M}$ ;  $n_1 = 47$ ,  $n_2 = 44$ ). **3**, Anthracene-9-carboxylic acid, 20 min ( $C = 0.45\text{ M}$ ,  $C_{\text{PIL-1}} = 1.45\text{ M}$ ;  $n_1 = 30$ ,  $n_2 = 37$ ). **4**, 3-cyanomethyl-1-vinylimidazolium bromide, 5 min ( $C = 0.47\text{ M}$ ,  $C_{\text{PIL-6}} = 1.5\text{ M}$ , methanol solvent;  $n_1 = 25$ ,  $n_2 = 25$ ). **5**, Ethyl viologen dibromide, 10 min ( $C = 0.24\text{ M}$ ,  $C_{\text{PIL-6}} = 1.17\text{ M}$ , methanol;  $n_1 = 43$ ,  $n_2 = 77$ ). **6**, *p*-Nitroaniline, 10 h ( $C = 2.90\text{ M}$ ,  $C_{\text{PIL-1}} = 2.42\text{ M}$ ;  $n_1 = 73$ ,  $n_2 = 33$ ). **7**, Tetrathiafulvalene, 5 min ( $C = 0.08\text{ M}$ ,  $C_{\text{PIL-3}} = 0.01\text{ M}$ , 1:1 v/v DCM/methanol;  $n_1 = 71$ ,  $n_2 = 90$ ). **8**, 1,2,4,5-Tetrakis(4-carboxyphenyl)benzene, 2 h ( $C = 0.05\text{ M}$ ,  $C_{\text{PIL-7}} = 0.04\text{ M}$ ;  $n_1 = 58$ ,  $n_2 = 36$ ). **9**, meso-tetra(carboxyphenyl)porphyrin, 10 min ( $C = 0.005\text{ M}$ ,  $C_{\text{PIL-1}} = 0.38\text{ M}$ ;  $n_1 = 35$ ,  $n_2 = 25$ ). **10**,  $\beta$ -Cyclodextrin, 10 h ( $C = 0.09\text{ M}$ ,  $C_{\text{PIL-1}} = 0.91\text{ M}$ ;  $n_1 = 26$ ,  $n_2 = 13$ ). **11**, Sodium iodide, 20 min ( $C = 0.47\text{ M}$ ,  $C_{\text{PIL-3}} = 1.51\text{ M}$ ;  $n_1 = 49$ ,  $n_2 = 57$ ). **12**, Phosphotungstic acid, 3 h ( $C = 0.06\text{ M}$ ,  $C_{\text{PIL-5}} = 0.71\text{ M}$ , water;  $n_1 = 11$ ,  $n_2 = 22$ ). **13**, Rhodium(I) tris(triphenylphosphine) chloride, 6 min ( $C = 0.04\text{ M}$ ,  $C_{\text{PIL-3}} = 0.49\text{ M}$ , DCM;  $n_1 = 35$ ,  $n_2 = 43$ ). **14**, Iron(III) meso-tetraphenylporphyrin chloride, 3 min ( $C = 0.02\text{ M}$ ,  $C_{\text{PIL-6}} = 1.17\text{ M}$ , DCM;  $n_1 = 43$ ,  $n_2 = 29$ ). **15**, Hen egg white lysozyme, 2 h ( $C = 0.002\text{ M}$ ,  $C_{\text{PIL-5}} = 1.83\text{ M}$ , NaAc-HAc buffer;  $n_1 = 21$ ,  $n_2 = 31$ ). **16**, Thaumatin, 16 h ( $C = 0.005\text{ M}$ ,  $C_{\text{PIL-5}} = 0.71\text{ M}$ , ADA buffer;  $n_1 = 99$ ,  $n_2 = 54$ ). **17**, CC3-R porous molecular cage, 10 min ( $C = 0.01\text{ M}$ ,  $C_{\text{PIL-3}} = 0.54\text{ M}$ , DCM;  $n_1 = 57$ ,  $n_2 = 47$ ). **18**, metal-organic polyhedron (MOP), 10 min ( $C = 0.003\text{ M}$ ,  $C_{\text{PIL-5}} = 1.42\text{ M}$ , methanol;  $n_1 = 40$ ,  $n_2 = 14$ ). **19**, HKUST-1 MOF grown from TA and  $\text{Cu}(\text{NO}_3)_2 \cdot 3\text{H}_2\text{O}$ , 10 h ( $C_{\text{TA}} = 0.27\text{ M}$ ,  $C_{\text{Cu}(\text{NO}_3)_2 \cdot 3\text{H}_2\text{O}} = 0.33\text{ M}$ ,  $C_{\text{PIL-4}} = 0.33\text{ M}$ ;  $n_1 = 32$ ,  $n_2 = 31$ ). **20**, TAPB-BTCA covalent organic framework, 15 min ( $C_{\text{TAPB}} = 0.02\text{ M}$ ,  $C_{\text{BTCA}} = 0.02\text{ M}$ ,  $C_{\text{PIL-1}} = 0.12\text{ M}$ , DMSO;  $n_1 = 112$ ,  $n_2 = 112$ ).



**Fig. 4 | Effects of shear rates and polymer's chain length on crystal growth.** **a**, Distributions of sizes of the TA crystals grown for 3 h from the same TA powder (not to be confused with experiments on growth from the oversaturated solutions presented in Figs. 1, 3) in PIL-1/DMF (PIL-1 molecular weight 402  $\text{kg mol}^{-1}$ ) under different mean shear rates. Each histogram is based on the analysis of (top to bottom panels) 1,000, 235, 100 and 131 crystals. **b**, Distributions of sizes of TA crystals grown for 3 h from the same TA powder under  $\dot{\gamma} = 85\text{ s}^{-1}$  mean shear rate in pure DMF (top panel), in monomer of PIL-1 in DMF (300 mg per 0.75 ml), and in PIL-1/DMF (300 mg per 0.75 ml) with two different molecular weights (indicated). Each histogram is based on the analysis of, top to bottom panels, 315, 348, 100 and 383 crystals. **c**, Equilibrium solubility (molar concentration at saturation) of TA in the same liquids as in panel **b**, measured with no shear. **d, e**, Measurements of viscosity at different shear rates. There is strong 'primary' shear thinning at low shear rates ( $10^{-4}\text{ s}^{-1}$  to  $10\text{ s}^{-1}$ , **d**), and a weaker 'secondary' shear thinning at higher shear rates ( $>10\text{ s}^{-1}$ , **e**), both are facilitated by addition of solvent (compare the blue curves measured for the same molecular weight of 402  $\text{kg mol}^{-1}$ , but at different concentrations, as indicated in the legend) or by increasing the molecular weight (compare orange curve of PIL-1 with molecular weight 849  $\text{kg mol}^{-1}$  at

concentration 300 mg per 0.75 ml DMF (same as in the crystal growth experiments) to dark blue curve for molecular weight 402  $\text{kg mol}^{-1}$  at 300 mg per 0.75 ml DMF (2 mM). As more solvent is added, the 'primary' shear thinning (**d**) progresses further into higher shear rates and reaches lower viscosities, indicating that disentanglement is limited by available solvent. In the high shear region (**e**), 'secondary' thinning also becomes more prominent when more solvent is added or when molecular weight is increased, and whenever a clear plateau could be discerned, onset of thinning (shown by black dots, which are intersections of dashed asymptotes) shifts to lower shears with more dilution ( $50\text{ s}^{-1}$  for 2 mM versus  $115\text{ s}^{-1}$  for 1 mM). For a more dilute, 1 mM sample, the 'secondary' thinning (**e**) begins at an even lower shear rate and merges into the first, low-shear thinning process, thus showing no clear plateau of viscosity. Curves from the yellow rectangle in **d** are plotted in **e** on a semi-logarithmic scale with viscosity  $\eta$  for each curve normalized by its value  $\eta_0$  at  $9\text{ s}^{-1}$ . Viscosity of pure DMF (grey dashed line) is taken from literature<sup>39</sup>. The curve for the monomer (green) is measured at higher concentration (2 g / 0.75 ml DMF) than for PILs, since more dilute monomer solution has even lower viscosity and could not be reliably measured by our rheometer.

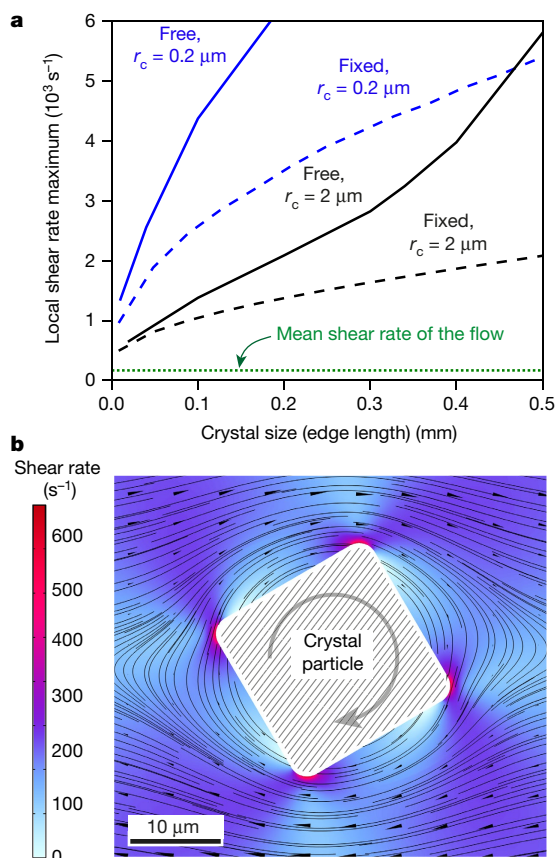


**Fig. 5 | Effects of particle size on local shear rates.** **a**, Maximum values of shear rate near an object (a rod as in panel **b**) in Couette flow ( $d = 1$  mm, mean  $\dot{\gamma} = 167$  s $^{-1}$  indicated by the horizontal dotted green line) as a function of the object's size and corner sharpness ( $r_c$  is the radius of corner curvature). Dashed curves were calculated for a non-rotating rod (with two of its faces kept parallel to the cell walls). Solid curves were calculated for a rod that is being freely rotated by the flow. **b**, Theoretical map of shear rate near a long, freely rotating rod in horizontal Couette flow (distance between walls  $d = 1$  mm, mean  $\dot{\gamma} = 167$  s $^{-1}$ ). The rod's axis points into the page; the rod's cross-section is a square (20  $\mu\text{m}$  per edge) with rounded corners ( $r_c = 2$   $\mu\text{m}$ ). Being freely rotated by the shear flow, the rod maintains a constant angular velocity (clockwise, as indicated by the circular grey arrow). Black curves are streamlines. Black cones indicate velocity direction and magnitude. This map depicts one instant of time; as the object rotates, maximal local shear rate oscillates in phase with this rotation, but regions of high shear rate remain mostly localized near the sharp corners at all times. The liquid is assumed to be newtonian, although very similar results were obtained when we used realistic dependence of viscosity on shear rate (from Fig. 4d, solid blue curve). Details of all these calculations are described in Supplementary Information section 4 (see also Supplementary

their effective volume of solvation layer<sup>30,31</sup> increases. This phenomenon is in line with previous experiments on both polymers and ionic liquids<sup>29</sup>, whereby adding more solvent enhances shear thinning, hinting that shear may cause greater demand for solvent by the polymer or ionic liquid; we found that this trend also holds for PIL-1/DMF (see blue curves in Fig. 4d). What this means for our experiments is that the disentangled polymers can effectively compete for solvent with the solute which, upon losing the solvent, starts to crystallize (this effect is loosely analogous to 'salting out', which causes the precipitation and crystallization<sup>32,33</sup> of various solutes, including biomolecules<sup>34,35</sup>). We observe that this mechanism explains why some other polymers are less robust or less general than PILs (such as PMMA and PVDF; see Fig. 2b, c), because they gelate or precipitate before the solute can develop large crystals. By contrast, PILs do not precipitate easily and are known to be versatile solvents, not unlike molten salts<sup>17,18</sup>.

The second part of the proposed mechanism rationalizes the preferential growth of larger (rather than smaller) crystals which, as we mentioned above in the context of crystal sizes increasing with viscosity and decreasing with solubility, cannot be ascribed to classical Ostwald ripening. Instead, the explanation might lie in the fact that in a mean shear flow, the local shear near a particle with sharp edges increases with particle size<sup>36,37</sup>. For our system, such an increase is supported by the results of computational fluid dynamics simulations of liquid flows around rod-shaped particles with square cross-sections ranging from 2  $\mu\text{m}$  to 1 mm and moving freely in a Couette cell (Fig. 5b, c). Therefore, the disentanglement of PILs and 'competition' for solvent are expected to be more pronounced near larger particles, which therefore grow preferentially; conversely, the smaller particles remain more soluble. Experimentally, we found that a mean shear of  $\dot{\gamma} = 167$  s $^{-1}$  indeed decreases global solubility of TA in PIL-1/DMF (molecular weight  $8.49 \times 10^5$  g mol $^{-1}$ ) from  $167.2 \pm 2.8$  mM to  $161.6 \pm 0.8$  mM (see Supplementary Table 1 in Supplementary Information section 2.1). We note that this 1%–5% modulation of solubility is an order of magnitude larger than the typical values sufficient to drive Ostwald ripening (for example, <0.1% for 10- $\mu\text{m}$  crystals of TA, assuming a surface energy of 100 mJ m $^{-2}$  in the Ostwald–Freundlich/Kelvin equation).

However, if it were just simple disentanglement or single-chain unfolding, it would have been reversible, and therefore some portion of crystals such as TA would re-dissolve shortly after stopping the rotation of the Couette cell: PIL-1 microstructure would have returned to its original state, releasing the captured solvent. In experiments, TA crystals did not re-dissolve even 15 h after the rotation had ceased, indicating that relaxation of PILs to the initial state is inhibited—perhaps owing to a gel-like macromolecular crowding in the concentrated solutions we use (this would be in line with onset of shear thinning already at very low shear rates  $<10^{-4}$  s $^{-1}$  shown in Fig. 4d, as well as linear response domain at very low strains (around 0.03) shown in the dynamic relaxation data in Supplementary Fig. 50a).

Finally, if the mechanism we propose for shear-enhanced ripening of powders (Fig. 2b, c and Fig. 4) is correct, it should also apply to the growth starting from oversaturated solutions (Fig. 1 and Fig. 3)—although, in the nucleation phase, it would strongly suppress smaller nuclei in favour of the larger ones, and we would expect large crystals to grow from such solutions faster than from powders. This is indeed the case and solution growth is approximately an order of magnitude faster. For instance, TA crystals reach a size of 440  $\mu\text{m}$  on average after 10 min of growth from solution (Fig. 1d) versus an average size of 336  $\mu\text{m}$  after only 3 h of growth from powder (Fig. 4a, bottom panel). Furthermore, the impact of this mechanism during nucleation phase must far outweigh the previously reported effects of shear flow on nucleation<sup>9–11,38</sup>, since those effects predict the negative effect of shear on the final crystal size—that is, the opposite of what we observe (Fig. 4a).

In summary, we showed that good-quality crystals of various kinds can grow larger and more rapidly when subject to shear in the presence of polymers. Since this trend is observed for crystals and polymers of various types, it can reasonably be explained by physical effects rather than the nuances of specific polymer–solute chemical interactions. At the same time, such interactions might have more subtle effects—we have seen, for instance, that linear PIL-1 and branched PIL-7 can give crystals of the same space group but different habits (see Supplementary Fig. 37). Such effects and also more detailed theoretical models certainly merit further study of this interesting non-equilibrium system. From a practical point of view, we anticipate that our technically straightforward, constant-temperature method will be useful as a means of accelerating crystal growth, especially for substances that must be kept within a narrow temperature range (for example, proteins) or cannot be recrystallized (such as metal–organic frameworks and covalent organic frameworks).

## Online content

Any methods, additional references, Nature Research reporting summaries, source data, extended data, supplementary information, acknowledgements, peer review information; details of author contributions and competing interests; and statements of data and code availability are available at <https://doi.org/10.1038/s41586-020-2042-1>.

1. Shekunov, B. Y. & York, P. Crystallization processes in pharmaceutical technology and drug delivery design. *J. Cryst. Growth* **211**, 122–136 (2000).
2. Variankaval, N., Cote, A. S. & Doherty, M. F. From form to function: crystallization of active pharmaceutical ingredients. *AIChE J.* **54**, 1682–1688 (2008).
3. Ulrich, J. & Froberg, P. Problems, potentials and future of industrial crystallization. *Front. Chem. Sci. Eng.* **7**, 1–8 (2013).
4. Censi, R. & Di Martino, P. Polymorph impact on the bioavailability and stability of poorly soluble drugs. *Molecules* **20**, 18759–18776 (2015).
5. Lee, E. H. A practical guide to pharmaceutical polymorph screening & selection. *Asian J. Pharm. Sci.* **9**, 163–175 (2014).
6. ICH Q6A Specifications: Test Procedures And Acceptance Criteria For New Drug Substances And New Drug Products: Chemical Substances Report CPMP/ICH/367/96 (European Medicines Agency, 2000); <https://www.ema.europa.eu/en/ich-q6a-specifications-test-procedures-acceptance-criteria-new-drug-substances-new-drug-products>.
7. *Guidance For Industry. ANDAS: Pharmaceutical Solid Polymorphism Chemistry, Manufacturing, And Controls Information* (Food and Drug Administration, 2007); [http://academy.gmp-compliance.org/guidemgr/files/POLYMORPHISM\\_7590FNL.PDF](http://academy.gmp-compliance.org/guidemgr/files/POLYMORPHISM_7590FNL.PDF)
8. Shamlou, P. A. & Titchener-Hooker, N. Turbulent aggregation and breakup of particles in liquids in stirred vessels. In *Processing of Solid-Liquid Suspensions 1–25* (Butterworth-Heinemann, 1993).
9. Wang, J. & Estrin, J. Secondary nucleation of sucrose by fluid shear in aqueous solutions. *Chem. Eng. Commun.* **152/153**, 275–286 (1996).
10. Forsyth, C. et al. Influence of controlled fluid shear on nucleation rates in glycine aqueous solutions. *Cryst. Growth Des.* **15**, 94–102 (2015).
11. Forsyth, C., Burns, I. S., Mulheran, P. A. & Sefcik, J. Scaling of glycine nucleation kinetics with shear rate and glass–liquid interfacial area. *Cryst. Growth Des.* **16**, 136–144 (2016).
12. Botsaris, G. D. Secondary nucleation—a review. In *Industrial Crystallization 3–22* (Springer, 1976).
13. McCabe, W. L., Smith, J. C. & Harriott, P. *Unit Operations Of Chemical Engineering* 1130 (McGraw-Hill, 1993).
14. Sung, C. Y., Estrin, J. & Youngquist, G. R. Secondary nucleation of magnesium sulfate by fluid shear. *AIChE J.* **19**, 957–962 (1973).
15. Andereck, C. D., Liu, S. S. & Swinney, H. L. Flow regimes in a circular Couette system with independently rotating cylinders. *J. Fluid Mech.* **164**, 155–183 (1986).
16. Hasell, T., Chong, S. Y., Jelfs, K. E., Adams, D. J. & Cooper, A. I. Porous organic cage nanocrystals by solution mixing. *J. Am. Chem. Soc.* **134**, 588–598 (2012).
17. Antonietti, M., Kuang, D., Smarsly, B. & Zhou, Y. Ionic liquids for the convenient synthesis of functional nanoparticles and other inorganic nanostructures. *Angew. Chem. Int. Ed.* **43**, 4988–4992 (2004).
18. Zhen, M., Yu, J. & Dai, S. Preparation of inorganic materials using ionic liquids. *Adv. Mater.* **22**, 261–285 (2010).
19. Gao, M. R., Yu, S. H., Yuan, J., Zhang, W. & Antonietti, M. Poly(ionic liquid)-mediated morphogenesis of bismuth sulfide with a tunable band gap and enhanced electrocatalytic properties. *Angew. Chem. Int. Ed.* **55**, 12812–12816 (2016).
20. Berry, G. C. & Fox, T. G. The viscosity of polymers and their concentrated solutions. *Fortsch. Hochpolym. Adv. Polymer Sci.* **5**, 261–357 (1968).
21. Szymański, J., Patkowski, A., Wilk, A., Garstecki, P. & Holyst, R. Diffusion and viscosity in a crowded environment: from nano-to macroscale. *J. Phys. Chem. B* **110**, 25593–25597 (2006).
22. De Gennes, P. G. Coil-stretch transition of dilute flexible polymers under ultrahigh velocity gradients. *J. Chem. Phys.* **60**, 5030–5042 (1974).
23. Cottrell, F. R., Merrill, E. W. & Smith, K. A. Conformation of polyisobutylene in dilute solution subjected to a hydrodynamic shear field. *J. Polym. Sci. A* **7**, 1415–1434 (1969).
24. Larson, R. G. *Constitutive Equations For Polymer Melts And Solutions* (Butterworth-Heinemann, 1988).
25. Link, A. & Springer, J. Light scattering from dilute polymer solutions in shear flow. *Macromolecules* **26**, 464–471 (1993).
26. Lee, E. C., Solomon, M. J. & Muller, S. J. Molecular orientation and deformation of polymer solutions under shear: a flow light scattering study. *Macromolecules* **30**, 7313–7321 (1997).
27. Smith, D. E., Babcock, H. P. & Chu, S. Single polymer dynamics in steady shear flow. *Science* **283**, 1724–1727 (1999).
28. Sun, J. K. et al. General synthetic route toward highly dispersed metal clusters enabled by poly(ionic liquid)s. *J. Am. Chem. Soc.* **139**, 8971–8976 (2017).
29. Burrell, G. L., Dunlop, N. F. & Separovic, F. Non-Newtonian viscous shear thinning in ionic liquids. *Soft Matter* **6**, 2080–2086 (2010).
30. Del Galdo, S. & Amadei, A. The unfolding effects on the protein hydration shell and partial molar volume: a computational study. *Phys. Chem. Chem. Phys.* **18**, 28175–28182 (2016).
31. Norman, A. I., Yiwei, F., Ho, D. L. & Greer, S. C. Folding and unfolding of polymer helices in solution. *Macromolecules* **40**, 2559–2567 (2007).
32. Noyes, A. A. The physical properties of aqueous salt solutions in relation to the ionic theory. *Science* **20**, 577–587 (1904).
33. Lewis, G. N. & Randall, M. *Thermodynamics And The Free Energy Of Chemical Substances* (McGraw-Hill, 1923).
34. Cohn, E. J. The physical chemistry of the proteins. *Physiol. Rev.* **5**, 349–437 (1925).
35. Miller, S. A., Dykes, D. D. & Polesky, H. A simple salting out procedure for extracting DNA from human nucleated cells. *Nucleic Acids Res.* **16**, 1215 (1988).
36. Schmid, D. W. Finite and infinite heterogeneities under pure and simple shear. PhD thesis, ETH Zurich (2002).
37. Nesbitt, W. S. et al. A shear gradient-dependent platelet aggregation mechanism drives thrombus formation. *Nat. Med.* **15**, 665–673 (2009).
38. Ramel, P. R., Campos, R. & Marangoni, A. G. Effects of shear and cooling rate on the crystallization behavior and structure of cocoa butter: shear applied during the early stages of nucleation. *Cryst. Growth Des.* **18**, 1002–1011 (2018).
39. Marcus, Y. *The Properties Of Solvents* (Wiley, 1998).
40. Chatterjee, S., Pedireddi, V. R., Ranganathan, A. & Rao, C. N. R. Self-assembled four-membered networks of trimesic acid forming organic channel structures. *J. Mol. Struct.* **520**, 107–115 (2000).

**Publisher's note** Springer Nature remains neutral with regard to jurisdictional claims in published maps and institutional affiliations.

© The Author(s), under exclusive licence to Springer Nature Limited 2020

# Article

---

## Data availability

All data used in the calculations are available in GitHub repository (<https://doi.org/10.5281/zenodo.3533635>).

## Code availability

All computer codes and COMSOL project files used in the calculations are available in GitHub repository (<https://doi.org/10.5281/zenodo.3533635>).

**Acknowledgements** We acknowledge support from the Institute for Basic Science Korea (Project Code IBS-R020-D1). We thank S. Lach for his help in the design and manufacture of the Couette cells, M. Siek for DLS measurements, C. Cahoon and K. K. Zheng

for rheological measurements, J. Yuan for help with PIL synthesis, and W. Adamkiewicz for discussions.

**Author contributions** J.-K.S. designed and performed most of the experiments. Y.I.S. developed theoretical models and helped with some experiments. W.Z. and Q.Z. synthesized most of the PIL polymers. B.A.G. conceived and supervised the research. All authors wrote the paper.

**Competing interests** A patent application based on these results has been submitted by the Institute for Basic Science (South Korea Patent Application 10-2019-0008413; inventors J.-K.S., Y.I.S. and B.A.G.).

## Additional information

**Supplementary information** is available for this paper at <https://doi.org/10.1038/s41586-020-2042-1>.

**Correspondence and requests for materials** should be addressed to B.A.G.

**Peer review information** *Nature* thanks Andrew Cooper, Laurence Noirez and the other, anonymous, reviewer(s) for their contribution to the peer review of this work.

**Reprints and permissions information** is available at <http://www.nature.com/reprints>.